Controlled plasma-droplet interactions: a quantitative study of OH transfer in plasma-liquid interaction

Gaku Oinuma[1,2], Gaurav Nayak[1], Yanjun Du[1,3] and Peter J Bruggeman[1]

[1]Department of Mechanical Engineering, University of Minnesota, 111 Church Street SE, Minneapolis, MN 55455, United States of America
[2]Advanced Technology R&D Center, Mitsubishi Electric Corporation, Hyogo 661-8661, Japan
[3]Institute for Plasma and Atomic Physics, Ruhr University Bochum, D-44780 Bochum, Germany

E-mail: pbruggem@umn.edu

July 2020

Abstract. Plasmas in contact with liquids are a rich source of OH radicals and have been extensively studied in the last decade to leverage the ability to generate chemically reactive species in gas phase plasmas to decompose organics. Multiphase transfer of OH radicals is highly transport limited and to overcome transport limits, the plasma activation of aerosols, small liquid droplets, interspersed in the plasma has been proposed. In this work, we report a combined experimental and modeling study of a controlled plasma-droplet interaction experiment using a diffuse RF glow discharge in He + 0.2% H_2O with detailed plasma diagnostics, *ex situ* analysis of the plasma-induced chemistry in the droplet containing formate, droplet trajectory and size measurements. This enables a quantitative study of the reactivity transfer of OH from the gas phase plasma to the liquid phase and how its diffusion limitations impact formate decomposition in the water droplet. For a droplet with a diameter of 36 μm, we observed 50% reduction in formate concentration in the droplets after plasma treatment for droplet residence times in the plasma of $\sim$10 ms. These short droplet residence times in the plasma allow in some cases for droplet size reductions of $\sim$5% in spite gas temperatures of 360 K. A one-dimensional reaction-diffusion model was used to calculate the OH transport and formate oxidation inside the droplet and was able to predict the conversion of formate by plasma in a droplet without any fitting parameters. The model further shows that formate conversion is dominated by near-interfacial reactions with OH radicals and is limited by diffusion of formate in the droplet. The results show that a controlled plasma-micro-droplet reactor as reported in this study might be an excellent tool for detailed quantitative plasma-liquid interaction studies.

Keywords: plasma-liquid interaction, droplet, atmospheric pressure plasma, OH radicals, plasma-induced liquid phase chemistry

1. Introduction

Plasmas in contact with liquids have been extensively studied in the last decade to leverage the ability to generate chemically reactive species in gas phase plasmas to produce chemical reactivity in the liquid phase [1]. The field of plasma-liquid interactions is underpinning many applications including water treatment and developments in the use for plasmas in medicine, agriculture and material synthesis [2]. Multiphase transfer of reactive species is typically transport limited. This is particularly the case for the treatment of liquids by plasmas. Transport must occur from the site of producing the reactive species in the gas phase plasma to the surface of the liquid, and subsequently into the liquid.

Several strategies have been pursued to overcome transport limits in plasma activating liquids– directly producing the plasma in the liquid [3], producing plasmas in bubbles in the liquid [4] and injecting plasma jets into the liquid [5]. Another strategy is the plasma activation of aerosols (small liquid droplets) interspersed in the plasma [6]. The plasma treatment of droplets or aerosols has many advantages compared to bulk liquid treatments with respect to overcoming transport limits. The distance from the site of production of a radical (or ion) due to electron impact processes in the gas to the droplet is shorter, enabling more rapid transport to the droplet. The surface-to-volume ratio of droplets, a few to tens of microns in size, is large, enabling more rapid transport into the liquid volume. Many low temperature plasma deposition processes of high functional coatings for energy and biotechnology applications rely on aerosol precursors [7, 8].

A large research effort in thermal plasma spraying has been devoted to the study of liquid precursors in plasma jets [9, 10]. As the gas temperature in these studies is typically >2000-3000 K, thermal effects dominate the plasma-droplet interactions resulting in full evaporation of the droplets. This is not the case for low temperature plasmas. The majority of fundamental studies on particles in low temperature plasmas have been performed in dusty plasmas (solid particles of a few to tens of micron size) at low pressure [11–13]. Particle charging has been intensively studied often for collisionless sheath conditions. The goal of these studies has been to characterize the dynamics of non-ideal plasmas and experiments have mainly been conducted in intrinsically non-reacting noble gases. Recent studies extend this work to reactive plasmas in the context of nanoparticle synthesis.

At atmospheric pressure, water sprays through plasmas have been used for the high efficiency production of H_2O_2 [6] and gold nanoparticles [14]. The deposition of

functional coatings using aerosol precursors in the plasma is also being studied [15]. Turner *et al* performed 3-dimensional simulations of the interaction of non-equilibrium atmospheric pressure plasmas with droplets containing precursors such as HMDSO for deposition purposes, with emphasis on the consequences of evaporation on the plasma properties [16]. More recently, the group of Kushner studied the effect of droplet size on the production of reactive oxygen and nitrogen species in droplets in air dielectric barrier discharges using 2D and 0-D plasma models [17]. Similarly, Machala *et al* studied the production of reactive nitrogen species by spark discharges during electro-sprayed droplets in the context of disinfection applications [18].

Maguire *et al* investigated aerosol charging in an RF driven plasma jet with the goal of achieving precision charging of micro-particles [19, 20]. They observed changes in particle size distributions and developed a model for particle charging. In their experiment, the nebulizer produces a large number of droplets ($\sim 10^5$/s) with a broad size distribution. The large volume of droplets has a strong impact on the plasma properties and the large range of droplet sizes makes it difficult to isolate size-dependent effects. Their coaxial plasma reactor produces an inhomogeneous plasma with possible large gradients in species and temperature gradients which results in some uncertainty in the plasma exposure of the droplet during its trajectory.

The unique and complex interactions of droplets with low temperature plasma are not well understood, and few quantitative experimental and modeling investigations have been reported. The work presented in this paper is a fundamental study of the interaction of plasma with droplets under well-controlled conditions using a droplet on demand system with fixed droplet size and a homogeneous plasma combined with detailed plasma diagnostics and *ex situ* analysis of the plasma-induced liquid phase composition changes.

Although correlations between plasma-induced liquid phase chemistry and plasma properties have been made [21–23], we currently have only a qualitative understanding of the dominant processes. The complex plasma-induced interfacial and near interfacial reactions have been modeled [17, 24] although no experimental validation of these models exist to date. Recent results also underline the importance of short-lived species in plasma-induced liquid phase processes [25, 26]. As short-lived species such as OH radicals have a limited penetration depth into the liquid [27], these species are only present on length scales of a few to tens of microns. Direct probing of the plasma-liquid interface is complex and can only be achieved for specific species for limited plasma conditions. An example is the measurement of solvated electrons by Go *et al* [28]. Hence an indirect analysis of the liquid reactivity itself combined with a comprehensive model is required to assess fluxes of reactive species to the droplet.

In this work, we present a study of the oxidation of sodium formate dissolved in micro-droplets by the plasma. This allows us, as will be shown in this paper, combined

with a one-dimensional transport model of OH radicals to study the reactivity transfer of OH from the gas phase plasma to the liquid phase. The combination of a well-controlled experimental condition with well-known and characterized plasma conditions allows for many modeling simplifications enabling a detailed comparison between model and experiment.

We conducted three types of experiments: (1) imaging of water droplets in plasmas to determine the residence time of the droplet inside the plasma including temporal changes of droplet diameter; (2) characterization of the plasma to quantify gas temperatures and gas phase OH and H_2O_2 densities; and (3) measurements of formate concentrations after the water droplets have been treated by the plasma. A newly constructed plasma reactor, described in section 2, which can generate a diffuse and steady-state atmospheric-pressure glow discharge with good optical accessibility, was used for these experiments. Section 3 shows the description of the one-dimensional model used to calculate the OH transport and formate oxidation inside the droplet. The experimental results are presented in section 4 and the detailed motivation of the model assumptions and the model outcomes are shown in section 5 before we present the discussion and conclusion.

2. Experimental setup and methods

2.1. Plasma reactor

Figure 1 provides a schematic drawing and a photograph of the plasma reactor used in this study. The plasma reactor is identical to the one used in [29]. The reactor was comprised of a pair of copper electrodes, a micro-droplet dispenser, and a droplet collector. The droplets released from the dispenser are carried by the gas flow through the RF-driven diffuse glow discharge generated between the electrodes before reaching the droplet collector. The gas flow is downwards in the direction of the gravitational force. The droplet collector was cooled down below the freezing point so that the droplets will freeze on the collector upon impact.

A pair of L-shaped copper electrodes form a parallel-plate discharge gap with an inter-electrode spacing of 2.1 mm and vertical and horizontal lengths of 9.5 and 19 mm, respectively. Inside each electrode was a water channel in which deionized water at a temperature of 293 K and an electrical conductivity of less than 0.5 μS/cm recirculates at a flow rate of 2 liters per minute to ensure a stable operating temperature of the plasma discharge during long duration measurement campaigns. The electrodes were fitted in a PTFE casing whose front and back surfaces were enclosed by quartz windows, allowing optical access to the plasma and droplets. The droplet dispenser (MicroFab Technologies Inc. MJ-ATP-01) was mounted on top of the casing. The tip of the dispensing device (the point from which the droplets are released) was

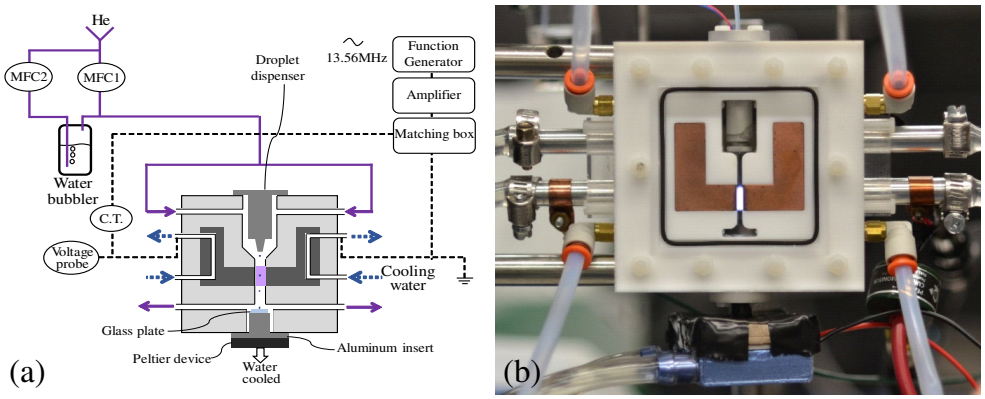

Figure 1. (a) Schematic of the experimental reactor, and (b) image of the plasma reactor with droplet dispensing and collector unit with plasma operated at 15W.

located 11.0 mm above the upper end of the electrodes. Two dispensing nozzles with different capillary diameters were used to generate droplets of 36-38 μm and 56 μm in diameter, respectively, at a given frequency controlled by an external driving unit (MicroFab Technologies Inc. CT-M5-01). The deviation of the diameter in continuous operation is less than 1 μm while the variability for experiments performed on different days is ± 2 μm, which has been confirmed by image analysis (see further). The droplet collector, located 7.2 mm below the lower end of the copper electrodes, is made of an aluminum insert. The upper side of the insert faces the plasma and the lower side is connected to a Peltier cooling device (LENX TES1-12704 Thermoelectric Cooler Peltier 30×30 mm^2) whose hot side is cooled by recirculating water. A 0.15 mm-thick glass plate (Bellco Glass Inc. 1943-00005) is placed on top of the insert with the aid of thermo-conductive silver paste. The temperature at the surface of the glass plate is maintained at about 260 K during the droplet experiments. The droplets released from the dispenser pass through the inert-electrode gap to be exposed to the plasma and are frozen on the glass plate upon impact.

Helium gas with a purity >99.999% was used and split into two gas lines, one line supplied dry helium, and the other provided water-saturated helium gas at room temperature generated by feeding the He gas through a water bubbler. The flow rate and water concentration were controlled by mass flow controllers (MKS GE50A). The gas inlet and outlet ports were located on both sides in the upper and lower portions of the reactor, respectively. A 1 m-long perfluoroalkoxy alkane (PFA) tube was connected to the gas outlet port and is open to ambient air at the far end. The long tube was used to suppress back diffusion of ambient air into the reactor. The reactor was mounted on a micrometer-controlled linear stage, which allowed us to

move it vertically with high precision for spatially resolved diagnostics along the path of the droplet through the reactor. In this study, the H_2O concentration in helium was fixed at 0.2%, while the total gas-flow rate varied between 0.5 and 1.5 slm.

The plasma was generated by a sinusoidal voltage waveform with a frequency of 13.56 MHz generated by a function generator (Tektronix AFG3022B) and amplified by an RF amplifier (E&I A150). A matching box (in house modified version of Vectronics HFT-1500) containing a π matching circuit was placed between the amplifier and the reactor to deliver the power efficiently from the amplifier to the plasma. A voltage probe (Tektronix P5100A) and a current transformer (Pearson Electronics, Model 2878) were placed at the powered RF connection between the matching box and the reactor. The acquired signals were recorded by an oscilloscope (Tektronix DPO2024B) and used to calculate the discharge power as described in [30]. By applying 13.56 MHz sinusoidal voltage, a homogeneous and steady diffuse glow discharge is generated. Figure 1(b) shows an image of the reactor with the plasma operating at a power of 15 W.

2.2. Imaging of droplets

The droplet images were recorded by a fast-framing camera (Photron FASTCAM Mini UX50) with a micro-focus lens (Nikon Micro-Nikkor 105 mm) and a 200 mm extension tube to obtain a high magnification. The camera was placed in front of the reactor, and an LED flashlight illuminated the droplets from behind. The video data were analyzed by image-analysis software (NIH ImageJ [31]) to determine the position, motion, and diameter of the droplets. The resolution of the image was 1.85 μm/pixel, and the frame rate and shutter speed were 10,000 frames per second (fps) and 3.9 μs, respectively. The camera setting and the intensity and position of the flashlight were kept unchanged throughout the work. The recorded video data were converted to a stack of 8-bit gray-scale still images for processing. By setting a threshold value, the images were converted to binary form to distinguish the droplets from the background. The area of the droplets was evaluated by counting the number of pixels shown in black. This also allowed us to calculate the diameter as no visual distortion of the droplets from their spherical shape has been observed in the plasma. The central position of the droplet was analyzed automatically by the software. The velocity of the droplet was calculated by comparing the center coordinates of two sequential images with a known frame rate. The original image size was 1,280×312 pixels, but only a cropped, well-focused area at the center was used to determine the droplet diameter. By moving the reactor vertically with the aid of the linear translation stage on which the plasma reactor was mounted, the data were recorded at different vertical locations to assess the variation of the droplet diameter and speed when moving from droplet dispensing to the droplet collector unit. Ten consecutive droplets were recorded by the fast-

framing camera, and the average diameter, velocity, and position were analyzed. The time elapsed in the plasma was calculated from the position and local velocity of the droplets, allowing us to evaluate the temporal changes of the droplet diameter.

In the droplet-imaging experiments, gas-flow rates of 0.5, 1.0 and 1.5 slm were adopted, which corresponded to the gas velocities of about 0.36, 0.71 and 1.06 m/s at the center of the discharge gap, respectively. The dispenser nozzle produced the droplets at a frequency of 20, 40 and 100 Hz in the cases of 0.5, 1.0 and 1.5 slm, respectively. Since the residence time of a droplet in the plasma was between 9 and 18 ms, only one droplet stayed in the plasma at a given moment. As will be shown later, the reduction in the droplet diameter in plasma was at most 5 μm, except for the 0.5 slm case operated at 15 W (8 μm). This loss of water from the droplet into the gas-phase plasma accounts for only a spatially averaged increase in water concentration of 0.004% in the plasma region at a gas flow rate of 1.5 slm and a dispensing frequency of 100 Hz. The impact of the droplet evaporation to the plasma was confirmed by imaging the plasma at different droplet dispensing frequencies of 100, 300 and 800 Hz, and at water concentrations of 0.2 and 0.3% in the feed helium gas using an iCCD camera (Andor iStar 340). The corresponding results are shown in Figure 2. A droplet dispensing frequency of 100 Hz does not impact the plasma emission significantly, however, at higher droplet generation frequencies ($\geq$300 Hz),

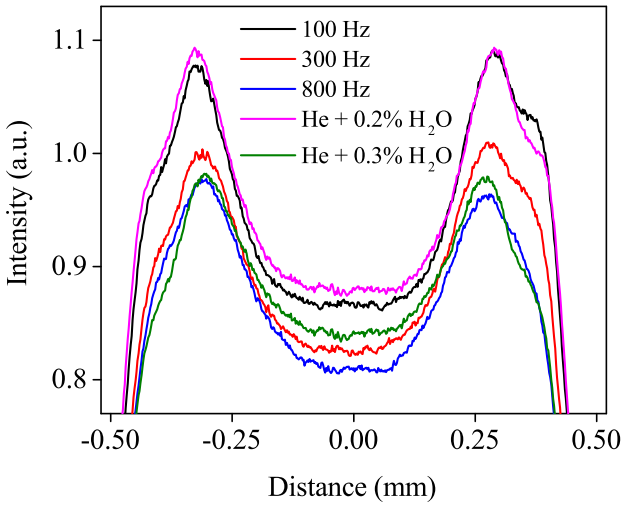

Figure 2. Spatially distributed plasma emission intensity at different droplet dispensing frequencies in a He + 0.2% H_2O discharge and at different water concentrations in helium without droplets. The plasma dissipated power was fixed at 15 W and a total gas flow rate of 1 slm was used.

the plasma emission becomes similar to emissions with 0.3% water content. At a higher dispensing frequency, e.g. 800 Hz, about 10 droplets stay in the plasma region at a given moment and they may account for the variation of the plasma emissions. It has been previously shown, however, that OH radical densities are not strongly dependent on small changes in the H_2O concentration in the RF discharge used [32], e.g. an increase of factor 2 in H_2O concentration only leads to 41% increase in the OH radical density. We have calculated the effect of an increase of 41% in OH density (3.5×10^{20} m^{-3}) on the formate decomposition in the droplet (see also further). The results show that the corresponding increase in formate decomposition is 6%. This variation is significantly less than the accuracy of the experiment.

2.3. Plasma characterization

The absolute-number density of OH was measured by the broadband UV-absorption technique as described in [32]. This technique also allows to measure the rotational temperature of the OH(X) ground state molecule which is a good representation of the gas temperature [33]. A broadband light source (Energetiq EQ-99 LDLS), a monochromator (ARC AM510) with a focal length of 1 meter equipped with a 1800 g/mm grating blazed at 500 nm, and a CCD camera (Andor iDus 420) were used for this measurement. The incident light was focused to about a 1 mm spot, and the measurement was performed at the center of the discharge gap at six vertical positions to obtain absorption spectra as a function of axial position in the plasma. The spectral resolution of the system was 25 pm FWHM at 310 nm. Four spectra were recorded at each measurement: background (L_{bg}); plasma emission (L_{p}); light source when plasma was on ($L_{\mathrm{p+l}}$); and light source when plasma was off (L_{l}). The absorption spectrum $A(\lambda)$ was obtained by the following equation:

$$A(\lambda) = 1 - \frac{L_{\mathrm{p+l}}(\lambda) - L_{\mathrm{p}}(\lambda)}{L_{\mathrm{l}}(\lambda) - L_{\mathrm{bg}}(\lambda)} = 1 - \frac{I(\lambda)}{I_0(\lambda)}, \tag{1}$$

where I and I_0 are the transmitted and reference light intensities, respectively. The computed absorption spectrum was fitted to the experimentally obtained spectrum based on the least-square scheme with the aid of a MATLAB Curve Fitting Toolbox to evaluate the temperature and number density as described in [34]. The fitting method also calculated the confidence intervals of the fitting parameters. The reported uncertainties in the gas temperature and OH density in this study represent 95% confidence intervals of the fitting. The OH density measurements have been performed in the center of the discharge gap at the location of the droplet trajectory.

For the quantification of gas-phase H_2O_2, the effluent gas from the reactor was bubbled in 15 mL of distilled water stored in a 50 mL measuring cylinder. In this setup, the gas-phase H_2O_2 was totally dissolved in the water, which was confirmed by separate experiments performed by changing the water volume and level.

The dissolved H_2O_2 concentrations were then measured by the colorimetric method using titanium oxysulfate as the reaction reagent as described in [35]. The volume averaged gas-phase H_2O_2 concentrations can be calculated from the dissolved H_2O_2 concentration for a given water volume (15 ml), gas-flow rate, and sampling time (20 min). The reported uncertainties in the H_2O_2 densities represent the standard deviation of three repeated measurements. The gas temperature and OH and H_2O_2 density measurements were performed without dispensing the droplets. The discharge power was fixed at 15±2 W throughout the study, and the gas-flow rates were set to 0.5, 1.0 and 1.5 slm.

2.4. Preparation of sample solution and quantification of formate

Sodium formate was chosen as the model organic substance in this study to evaluate the interaction between plasma and water droplet. Sodium formate is quickly degraded by reaction with OH while O_3 and H_2O_2 have limited impact on formate, hence this substance is very suitable for studying the effect of short-lived species as OH. The simple molecular structure and well-known chemistry of formate are advantageous and enables us to develop a numerical model of the liquid phase chemistry [36, 37]. A 2 mM sodium formate solution was prepared by mixing equimolar amounts of formic acid and sodium hydroxide and dissolving into distilled water. The formate concentrations were quantified by the Formate Assay Kit (MAK059, Sigma Aldric) based on enzymatic reactions producing colorimetric products having a strong absorbance at 450 nm, proportional to the formate concentration. Apart from some initial measurements which were performed with a plate reader (Synergy H1 microplate reader, BioTek Instruments, Inc.), all formate concentration measurements were performed using broadband absorption spectroscopy, which led to a reduced variability of the measurements.

For the formate-degradation experiments, the gas-flow rates were set to 0.75, 1.0, and 1.5 slm to change the residence times of the droplets in the plasma. The droplet dispensing frequencies were 1000 and 300 Hz for the droplet sizes of 36 and 56 μm, respectively to ensure sufficient collected liquid volumes for the *ex situ* measurement of formate. The sampling was performed for 5 minutes in both conditions, which allowed us to collect between 7 and 9 μl of sample solution. The collected sample was carefully washed out from the glass plate on the droplet collector using 200 μl of the buffer solution of the Formate Assay Kit. The diluted sample was then transferred to a 96-well plate for the absorption measurements. Three cells, each containing 50 μl, were used for triplicate measurements, and the average and standard deviation were evaluated. For broadband absorption measurements, the collected sample was washed out with 140 μl of distilled water into 96-well plate. The diluted sample was mixed with 100 μl of buffer solution and reaction mix from the Formate Assay Kit, incubated

at 37°C for an hour, transferred to a micro-cuvette and absorbance was measured at 450 nm. The validity of both these methods was confirmed by operating the whole procedure without generating the plasma, which yielded a formate concentration in the collected sample of ±10.3% of the initial concentration. All measurements have been performed in triplicates and the reported uncertainty represents the standard deviation.

3. Description of the 1D diffusion-reaction model

3.1. Model overview

The following key assumptions have been made and enabled the use of a 1D reaction-diffusion model to calculate the plasma-induced oxidation of formate in the droplet:
Assumption 1: OH and H_2O_2 are the dominant species entering the droplet in the plasma and the role of other gas phase species in the oxidation of sodium formate can in first approximation be neglected.
Assumption 2: Evaporation of the droplet in the plasma can be neglected and the droplet temperature remains close to 300 K.
Assumption 3: OH and H_2O_2 diffuse from the bulk plasma to the droplet and decomposition reactions can be neglected during that process for the investigated experimental conditions.
Assumption 4: Convection inside the droplet does not significantly impact the oxidation of sodium formate.

These assumptions will be motivated in detail based on experimental data in the results section for the specific measurement conditions reported in this work. Figure 3 illustrates the concept of the 1D reaction-diffusion model. The droplet was assumed to be exposed to the measured OH and H_2O_2 density present in the bulk plasma for the duration of the measured droplet residence time in the plasma. The model assumes a homogeneous plasma with the assumption of the near droplet boundary layer and only considers the radial transport of OH and H_2O_2 into the droplet. The droplet transit through the plasma is accounted for in the model by the time dependence of droplet exposure to the plasma species. As the sodium formate solution is stored in a glass bottle in ambient air before supplying to the dispenser, the dissolved O_2 concentration of the solution is in equilibrium with air (21%). In the reactor, O_2 is considered an impurity and has the same impurity level as that of the helium gas (i.e. 5 ppm), so a droplet experiences a significant reduction of O_2 partial pressure when entering the reactor and the model considers the transfer of dissolved O_2 from the liquid interface back into the gas phase.

The governing equation for an aqueous species was described by the one-

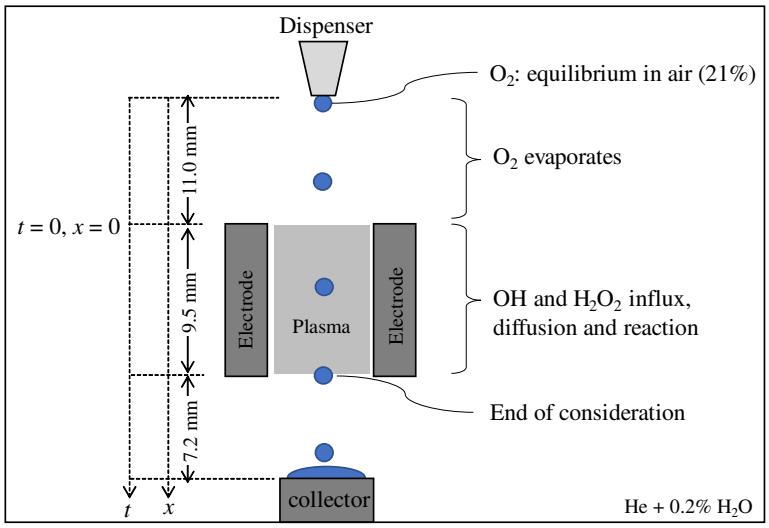

Figure 3. Concept of the model and coordinate system.

dimensional reaction-diffusion equation in spherical coordinates:

$$\frac{\partial A_\mathrm{j}}{\partial t} = D_{\mathrm{l,j}} \left(\frac{2}{r} \frac{\partial A_\mathrm{j}}{\partial r} + \frac{\partial^2 A_\mathrm{j}}{\partial r^2} \right) + \Sigma_\mathrm{i} k_\mathrm{ij} A_\mathrm{i} A_\mathrm{j}, \tag{2}$$

where A_j is the aqueous concentration of the species j in consideration, $D_{\mathrm{l,j}}$ is the aqueous diffusion coefficient of species j in the droplet, r is the radial position in the droplet, and $\Sigma_\mathrm{i} k_\mathrm{ij} A_\mathrm{i} A_\mathrm{j}$ is the sum of all reaction rates involving species j in the droplet with reaction rate coefficient k_ij. Fifteen aqueous species (OH, H_3O^+, OH^-, H_2O, O_2, H_2O_2, HO_2, O_2^-, O^-, O_3^-, HO_2^-, HCOOH, COO^-, $HCOO^-$, and HCOO) are considered in this model corresponding to a set of 15 coupled differential equations that were numerically solved with boundary conditions as described below by a finite difference scheme with time and spatial steps of 5 ns and 18 nm, respectively.

3.2. Boundary conditions

The symmetric boundary condition at the center of the droplet was taken as:

$$D_\mathrm{l} \left[\frac{\partial A}{\partial r} \right]_{r=0} = 0. \tag{3}$$

For the boundary condition at the plasma-droplet interface, we adopted three descriptions depending on the species. In the case of O_2, we assume that the aqueous concentration at the interface in the liquid is in equilibrium with the ambient O_2 gas concentration (assumed 5 ppm):

$$A_{r=R_\mathrm{p}} = HG_\infty \tag{4}$$

with R_p the droplet radius, H the Henry's constant, and G_∞ the steady-state O_2 concentration in the gas phase. The mass continuity of OH and H_2O_2 at the droplet interface is taken from the uptake model reported in [38] and includes gas and liquid phase diffusion, mass accommodation and Henry's law:

$$D_\mathrm{g}\left(\frac{\partial G}{\partial r}\right)_{r=R_\mathrm{p}} = \frac{1}{4}\alpha v_\mathrm{th}\left[G\left(R_\mathrm{p},t\right) - \frac{A\left(R_\mathrm{p},t\right)}{H'}\right] = D_\mathrm{l}\left(\frac{\partial A}{\partial r}\right)_{r=R_\mathrm{p}}, \quad (5)$$

for which G is the gas-phase concentration of OH or H_2O_2, D_g the diffusion coefficient in the gas phase, α the mass accommodation coefficient at the droplet interface, v_th the mean speed of the molecule in gas phase and H' the dimensionless Henry's constant defined as

$$H' = HRT, \quad (6)$$

where R and T represent the ideal gas constant and gas temperature, respectively. As the droplet size is more than an order of magnitude smaller than the plasma in the interelectrode gap (2.1 mm), we consider the OH and H_2O_2 gas density profile to be equal to the steady-state diffusion profile in the gas of a spherical droplet in an infinite gas environment [38]

$$G(r,t) = G_\infty - \frac{R_\mathrm{p}}{r}\left[G_\infty - G\left(R_\mathrm{p},t\right)\right]. \quad (7)$$

Differentiating (7) with respect to r yields

$$\frac{\partial G(r,t)}{\partial r} = \frac{R_\mathrm{p}}{r^2}\left[G_\infty - G\left(R_\mathrm{p},t\right)\right]. \quad (8)$$

Hence, the molecular flux at the interface can be written as

$$D_\mathrm{g}\left(\frac{\partial G}{\partial r}\right)_{r=R_\mathrm{p}} = \frac{D_\mathrm{g}}{R_\mathrm{p}}\left[G_\infty - G\left(R_\mathrm{p},t\right)\right]. \quad (9)$$

By equating (5) and (9), the gas-phase concentration at plasma-droplet interface is given by

$$G(R_\mathrm{p},t) = \frac{R_\mathrm{p}\alpha v_\mathrm{th}}{H'(R_\mathrm{p}\alpha v_\mathrm{th} + 4D_\mathrm{g})}A(R_\mathrm{p},t) + \frac{4D_\mathrm{g}G_\infty}{R_\mathrm{p}\alpha v_\mathrm{th} + 4D_\mathrm{g}}. \quad (10)$$

Substituting (10) into (5), one can express the droplet interface boundary condition for OH and H_2O_2 as follows:

$$D_\mathrm{l}\left(\frac{\partial A}{\partial r}\right)_{r=R_\mathrm{p}} = a_1 A(R_\mathrm{p},t) + a_2, \quad (11)$$

with

$$a_1 = -\frac{\alpha v_\mathrm{th} D_\mathrm{g}}{H'(R_\mathrm{p}\alpha v_\mathrm{th} + 4D_\mathrm{g})}, \quad (12)$$

$$a_2 = \frac{\alpha v_\mathrm{th} D_\mathrm{g} G_\infty}{R_\mathrm{p}\alpha v_\mathrm{th} + 4D_\mathrm{g}}. \quad (13)$$

Table 1. Gas-phase diffusion coefficients, dimensionless Henry's constants and mass accommodation coefficients of OH, H_2O_2 and O_2.

	OH	**H_2O_2**	**O_2**
$D_g^{\dagger}$	0.847 [39]	0.566‡ [40]	
H' [41]	661.8	1.98×10^6	0.0289
A	0.83 [42]	0.109 [43]	

†Value corresponds to the coefficients in helium at 300 K.

‡Diffusivity of HO_2 in He was used as the data was not available for H_2O_2.

The gas-phase diffusion coefficients, dimensionless Henry's constants and mass accommodation coefficients of O_2, OH, and H_2O_2 are listed in Table 1. For all other aqueous species considered, total reflection (no mass transfer) was considered as the boundary condition at the droplet interface. We used the measured H_2O_2 and steady-state OH density for G_∞ to calculate the gas-droplet boundary condition.

3.3. Reaction mechanism

The reaction mechanism in the droplet we adopted is compiled in Table 2 [36, 37]. Consistent with our initial assumptions, we neglected the reactions involving H atoms and solvated electrons (e_{aq}^-) due to their minor impact and contributions to OH-initiated aqueous chemistry. We also did not consider reactions of CO_2 and carbonic acid as this study is not focused on the reaction products of the oxidation process and the concentrations remain well below the formate concentration making their relative importance for quenching OH radicals negligible as compared to the reaction of OH with formate.

4. Experimental results

4.1. Plasma properties

Figure 4 shows the voltage and current waveforms of the He + 0.2% H_2O RF glow discharge operating at 15 W. The peak voltage and current were about 460 V and 0.5 A, respectively. As shown in Figure 1(b), the plasma filled the entire gap between the two electrodes at 15 W, while a reduced plasma size was visually observed at the top and bottom ends of the electrodes in the case of 10 W.

Figure 5 shows the gas temperature as a function of the vertical position at 15 W at gas flow rates of 0.5, 1.0, and 1.5 slm. The temperature increases along the gas flow direction and saturates between 350 and 360 K. The gas temperature seems to decrease at the lower edge of the plasma, although the uncertainty in the gas temperature determination increases at that position due to the significant reduction

Table 2. Reaction mechanisms used in the model.

No.	Reaction	Rate coefficient[a]	Ref.
R1	$OH + HO_2 \rightarrow H_2O + O_2$	1×10^{10}	[36]
R2	$OH + OH \rightarrow H_2O_2$	4×10^{9}	[36]
R3	$OH + H_2O_2 \rightarrow HO_2 + H_2O$	3.3×10^{7}	[36]
R4	$OH + OH^- \rightarrow H_2O + O^-$	1.2×10^{10}	[36]
R5	$OH + O^- \rightarrow HO_2^-$	2.7×10^{10}	[36]
R6	$OH + O_2^- \rightarrow OH^- + O_2$	9.1×10^{9}	[36]
R7	$OH + HO_2^- \rightarrow OH^- + HO_2$	7.5×10^{9}	[36]
R8	$OH^- + H_3O^+ \rightarrow 2H_2O$	3×10^{10}	[36]
R9	$HO_2 (+ H_2O) \rightarrow H_3O^+ + O_2^-$	1×10^{6} s^{-1}	[36]
R10	$H_3O^+ + O_2^- \rightarrow HO_2 + H_2O$	5.7×10^{10}	[36]
R11	$2H_2O \rightarrow OH^- + H_3O^+$	5.5×10^{-6} s^{-1}	[36]
R12	$H_2O + O^- \rightarrow OH^- + OH$	1.8×10^{6}	[36]
R13	$O^- + HO_2^- \rightarrow O_2^- + OH^-$	4×10^{8}	[36]
R14	$O_2 + O^- \rightarrow O_3^-$	3.5×10^{9}	[36]
R15	$O^- + O_2^- (+ H_2O) \rightarrow 2OH^- + O_2$	6×10^{8}	[36]
R16	$H_2O_2 + O^- \rightarrow O_2^- + H_2O$	5×10^{8}	[36]
R17	$H_2O_2 + HO_2 \rightarrow O_2 + H_2O + OH$	5.3×10^{2}	[36]
R18	$H_2O_2 + O_2^- \rightarrow O_2 + OH + OH^-$	1.6×10^{1}	[36]
R19	$H_3O^+ + O^- \rightarrow OH + H_2O$	1×10^{10}	[36]
R20	$HO_2^- + O_3^- \rightarrow OH^- + O_2 + O_2^-$	8.9×10^{5}	[36]
R21	$O^- + O^- (+ H_2O) \rightarrow OH^- + HO_2^-$	1×10^{9}	[36]
R22	$HO_2^- + H_2O \rightarrow H_2O_2 + OH^-$	1.1×10^{6}	[36]
R23	$OH^- + HO_2 \rightarrow O_2^- + H_2O$	1×10^{10}	[36]
R24	$H_2O_2 + OH^- \rightarrow HO_2^- + H_2O$	1×10^{10}	[36]
R25	$O^- + O_3^- \rightarrow 2O_2^-$	7×10^{9}	[36]
R26	$H_3O^+ + HO_2^- \rightarrow H_2O_2 + H_2O$	3×10^{10}	[36]
R27	$HO_2 + HO_2 \rightarrow H_2O_2 + O_2$	2×10^{6}	[36]
R28	$H_2O_2 + O_3^- \rightarrow O_2 + O_2^- + H_2O$	1.6×10^{6}	[36]
R29	$O_2^- + HO_2 \rightarrow O_2 + HO_2^-$	5×10^{7}	[36]
R30	$H_2O_2 (+ H_2O) \rightarrow HO_2^- + H_3O^+$	3×10^{1} s^{-1}	[36]
R31	$OH + HO_2^- \rightarrow H_2O + O_2^-$	7×10^{9}	[36]
R32	$OH + O_3^- \rightarrow HO_2 + O_2^-$	8.5×10^{9}	[36]
R33	$H_3O^+ + O_3^- \rightarrow O_2 + OH + H_2O$	9×10^{10}	[36]
R34	$O_3^- \rightarrow O_2 + O^-$	4.3×10^{3} s^{-1}	[36]
R35	$HCOOH + OH \rightarrow HCOO + H_2O$	1.3×10^{8}	[37]
R36	$HCOO^- + OH \rightarrow COO^- + H_2O$	3.2×10^{9}	[37]
R37	$HCOO + O_2 \rightarrow CO_2 + HO_2$	3×10^{9}	[37]
R38	$COO^- + O_2 \rightarrow CO_2 + O_2^-$	2.4×10^{9}	[37]
R39	$HCOOH (+ H_2O) \rightarrow HCOO^- + H_3O^+$	1×10^{1}	[36]
R40	$HCOO^- + H_3O^+ \rightarrow HCOOH + H_2O$	5.65×10^{4}	[36, 37]

[a]Rate coefficients have units of $M^{-1}s^{-1}$ unless stated otherwise.

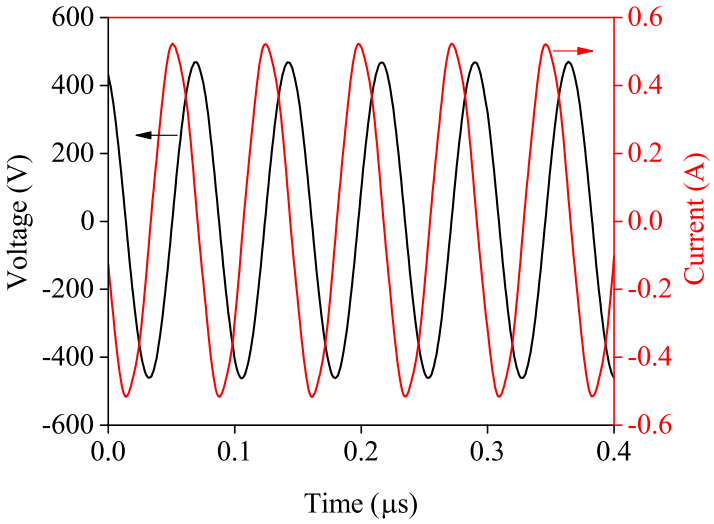

Figure 4. Voltage and current waveforms of the discharge operating in He + 0.2% H_2O at 15 W.

in the OH absorption signal corresponding to a reduction in OH density at the edge of the plasma. The gas flow rate did not strongly affect the steady-state temperature, while the distance to reach steady-state became smaller with reducing gas flow rates. The increase in gas temperature in the direction of the gas flow can be fitted by exponential functions as shown in Figure 5. For fitting the exponential curves, the temperature at the upper end (x = 0 mm) is assumed to be room temperature, and the last measurement point has been excluded from the fit due to the large uncertainty in the gas temperature values at this position.

Figure 6(a) and Figure 6(b) show the OH and H_2O_2 number densities measured at a constant power of 15 W and gas flow rates of 0.5, 1.0, and 1.5 slm, respectively. The OH densities increase along the gas flow direction, reaching a steady-state value after 3 mm in the plasma, and drop significantly at the lower edge of the plasma. This is consistent with the short lifetime of the OH radical which is much smaller than the smallest gas residence time used in this study (7.44 ms). This confirms that the exposure of the droplet to OH radicals is mainly confined to the time when the droplet resides in the plasma. The steady-state OH density was 3×10^{20} m^{-3} and independent of the gas flow rate between 0.5 and 1.5 slm. The H_2O_2 densities, calculated from the collected H_2O_2 in water downstream of the reaction, were between 3 and 6×10^{19} m^{-3} and increased at increasing gas flow rates. This is consistent with the reported results by Vasko *et al* [44] and is due to a reduction of gas residence time, which coincides with a reduction in the destruction of the produced H_2O_2 in the discharge by short-lived

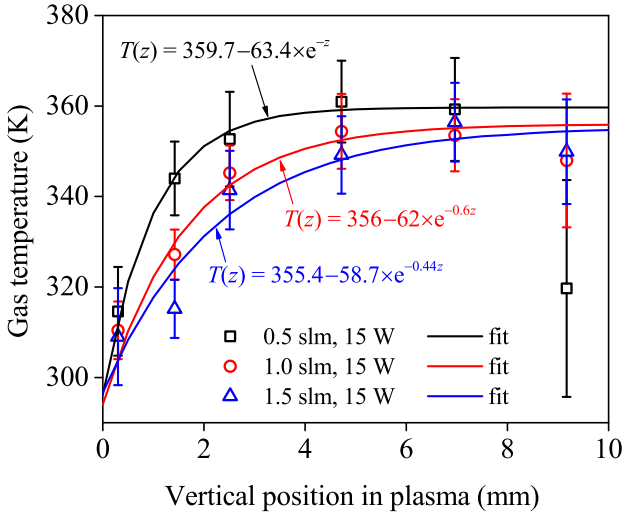

Figure 5. Gas temperatures as a function of the vertical position in the plasma. The zero position corresponds to the upper edge of the electrode.

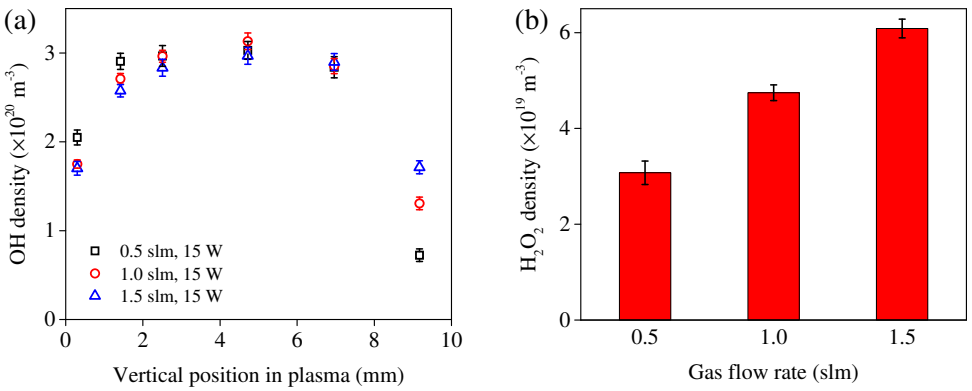

Figure 6. (a) OH number densities as a function of the vertical position in the plasma for different gas flow rates, and (b) H_2O_2 number densities obtained through measuring the H_2O_2 production in the effluent as a function of gas-flow rate.

species such as OH radicals.

4.2. Droplet behavior in plasma

The position and size of the droplet are monitored by microscopic fast framing imaging as described in Section 3 to determine the residence time and variation in droplet

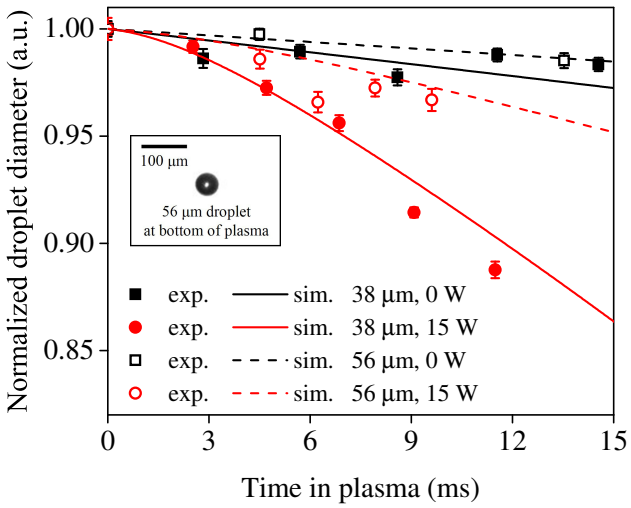

Figure 7. Variations of droplet diameters in plasma as a function of residence time in the plasma for a gas flow rate of 1 slm and discharge power of 15 W for droplet diameters of 38 μm and 56 μm. The reduction in droplet diameters is simulated using a droplet evaporation model (see text for details). The insert shows a droplet image for a 56 μm droplet recorded at the bottom of plasma for the same operating conditions.

diameter due to evaporation inside the plasma. Figure 7 shows the temporal variations of the droplet diameters with respect to the droplet residence time in the plasma for two different droplet diameters at the time of droplet generation (38 μm and 56 μm). The first and last points in the horizontal axis correspond to the data at the upper and lower ends of the plasma, respectively. The last reported measurement point equals the residence time of the droplet in the plasma. The vertical axis is normalized with the droplet diameter at x = 0. For all conditions we examined, droplet-size reductions due to evaporation were observed. For a 38 μm droplet, the size reduction became more pronounced when the plasma was generated. The diameter decreased by a few percent when the plasma was off, while about 11.2% reduction in droplet diameter was observed in the case of 15 W at a flow rate of 1 slm. The gas flow rate and the initial droplet size also affected the reduction of the diameter. The reduction rate of the droplet diameter increases with reducing gas flow rate and droplet diameter. The gas residence time, droplet diameter reduction and corresponding percentage of volume reduction for different conditions are reported in Table 3. Imaging using the fast framing camera shows that the droplets have a spherical shape without notable distortion within the plasma, and the resolution of the images is sufficiently high to evaluate changes in diameter (also shown in Figure 7).

Table 3. Droplet conditions for two initial droplet diameters at different gas flow rates, droplet residence time (t_{res}), reduction in diameter and maximum evaporation (by volume) at a discharge power of 15 W.

Droplet diameter [μm]	Gas flow rate [slm]	t_{res} [ms]	Droplet diameter reduction [%]	Volume reduction [%]
	0.5	17.45	21.9	52.4
38	1.0	11.49	11.2	30.1
	1.5	8.44	6.4	18.1
	0.75	11.50	4.7	13.3
56	1.0	9.50	5.8	16.3
	1.5	7.44	5.1	14.4

The reduction of the droplet as a function of the droplet residence time in the plasma can be estimated by an evaporation model that describes the evaporation process of a droplet in a homogeneous gas with a given temperature. The important processes that strongly impact the droplet evaporation are the heat transfer from the gas to the droplet that needs to supply the energy required for the latent heat of evaporation and the diffusion of water from the droplet to the surrounding as it impacts the relative humidity at the droplet-gas interface and, hence, can slow down evaporation. Using the approach of [45], we can describe the two processes expressing mass continuity and energy conservation:

$$T_{\mathrm{s}} = T_{\infty} - \frac{DML}{R_{\mathrm{A}}K}\left(\frac{P_{\infty}}{T_{\infty}} - \frac{P_{\mathrm{s}}}{T_{\mathrm{s}}}\right) \tag{14}$$

$$\frac{d(d_{\mathrm{p}})}{dt} = \frac{4DM}{R_{\mathrm{A}}\rho d_{\mathrm{p}}}\left(\frac{P_{\infty}}{T_{\infty}} - \frac{P_{\mathrm{s}}}{T_{\mathrm{s}}}\right) \tag{15}$$

with T_{s}, the temperature at the droplet surface, T_{∞} the homogenous plasma gas temperature, P_{s} the water vapor pressure at droplet surface, P_{∞} the homogeneous water vapor pressure, L the latent heat of water vaporization, M the molecular weight of water, K the thermal conductivity of helium, ρ the liquid density of water and d_{p} the droplet diameter.

The good correspondence of the experiments with the outcome of the model using the measured gas temperature as input, as shown in Figure 7 for two different initial droplet diameters (38 μm and 56 μm), suggest that other possible droplet heating mechanisms such as electron-ion or radical recombination reactions as reported by Maguire *et al* [19] do not strongly contribute to the evaporation process for the experimental conditions in the present study.

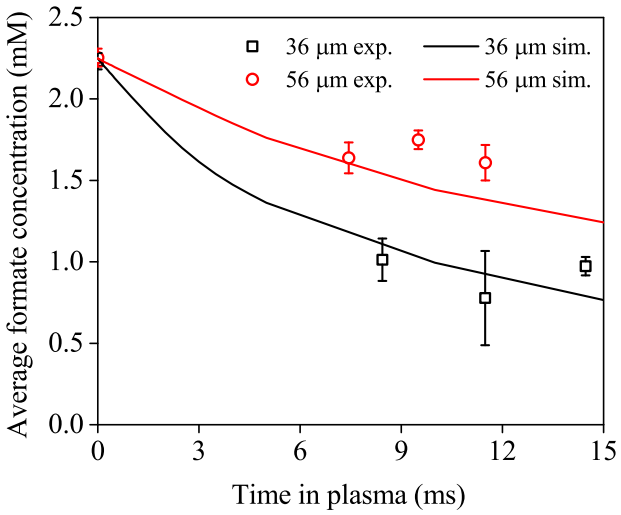

Figure 8. Formate concentration after droplet exposure to plasma as a function of droplet residence time for an initial droplet diameter of 36 μm and 56 μm. The discharge power was fixed at 15±2 W, while the gas flow rates were set to 0.75, 1.0, and 1.5 slm to vary the residence time of the droplets in the plasma.

4.3. Formate degradation

Figure 8 shows the formate concentrations in droplets with an initial diameter of 36 μm and 56 μm as a function of different droplet residence times inside the plasma, achieved by employing different feed gas flow rates. The formate concentration decreased by about 28% from the initial concentration of 2.25 mM in the case of 56 μm droplets, while in the case of 36 μm droplets, the concentration reduced by more than 50%. This result shows that the treatment of smaller sized droplets having an increased surface-to-volume ratio improves the oxidation of formate by the plasma. The residence times for the 56 μm droplets were slightly shorter in comparison with those of the 36 μm droplets. This is because the initial droplet velocity upon release from the dispenser nozzle differed slightly for the various droplet sizes. A detailed analysis of this formate treatment result will be provided by comparing the experimental conversion of formate with the model results in the next section.

5. Modeling results

5.1. Motivation of model assumptions

Assumption 1: OH *and* H_2O_2 *are the dominant species entering the droplet in the plasma and the role of other gas phase species in the oxidation of sodium formate can*

in first approximation be neglected.

0-D kinetic models of the He-H_2O RF glow discharge show that the dominant neutral species are H, OH and H_2O_2 [46]. As the H_2O dissociation remains small in this diffuse glow discharge, the O density remains significantly lower than the H and OH densities. In addition, O has also a lower Henry's law constant than OH and hence, any oxidation effects induced by O will be dominated by OH radical-induced oxidations [47]. We can also neglect the effect of H radicals on formate decomposition as the Henry's law constant of H is 5 orders of magnitude smaller than that of OH [41] and the reaction rate coefficient of H with formate is smaller than that for OH [48]. Nonetheless, in addition to diffusion of gaseous OH to the droplet, there are two other possible important sources of OH at the droplet-plasma interface: VUV photolysis and ion conversion/hydration reactions at the plasma-liquid interface such as $H_2O^+ + H_2O \rightarrow H_3O^+ + OH$. As all experiments have been performed with 0.2% H_2O and He excimer production is quickly quenched by impurities, VUV photolysis can in good approximation be neglected [49]. In spite that the electron/ion density is 3 orders of magnitude smaller than the OH density [46], fluxes of charged and neutral species can be significant and need to be estimated before any conclusions can be made. Furthermore, H_2O_2 is a long-lived species and the transfer of gas-phase H_2O_2 occurs inside the active plasma, in the afterglow and can even occur after the droplet is collected on the collection surface. This makes it very difficult to assess the origin of the experimentally measured liquid-phase H_2O_2 in the collected droplets. Therefore, a direct comparison of H_2O_2 concentration between the model and experiment cannot be done in our setup.

First, we estimate the equilibrium concentration of the OH density from Henry's law which is $\sim 4\times10^{-4}$ M with a gas phase density of 3×10^{20} m^{-3}. This value is significantly larger than the calculated OH density at the liquid-gas interface in the model, showing that the fast reactions of the OH radical do not lead to a limitation of the influx by the limitations imposed by Henry's law. Hence, we can calculate the OH flux as follows:

$$\Gamma_{OH} \approx \frac{1}{4}\alpha G_{OH} v_{th} \times 4\pi R_p^2 \approx 2 \times 10^{14} \text{ s}^{-1} \tag{16}$$

The ion flux can be approximated by the electron flux as follows:

$$\Gamma_{ion} \approx \Gamma_e \approx \frac{1}{4} n_e \overline{v}_e \times 4\pi R_p^2 \exp\left(\frac{q\phi}{kT_e}\right) \approx 2 \times 10^{12} \text{ s}^{-1} \tag{17}$$

To obtain the ion flux, we assume that the droplet potential (ϕ) is $\sim$4 times the electron temperature ($< T_e > \sim 3$ eV) and the electron density is 10^{17} m^{-3} [32, 50]. The ion flux is two orders of magnitude smaller than the OH flux allowing us to neglect in first approximation the production of OH at the droplet interface by ion impact.

Solvated electrons are also able to dissociate formate with a rate constant of 8×10^3 M^{-1}s^{-1}, which is several orders smaller than that of OH dissociation. As the

electron flux is two orders of magnitude lower than the OH flux and the liquid phase penetration depth of e^- is orders of magnitude smaller than OH [28] due to its higher reactivity, we can also neglect electron-induced dissociation of formate in the present study.

Assumption 2: *Evaporation of the droplet in the plasma can be neglected and the droplet temperature remains close to 300 K.*

The maximum reduction in droplet diameter for the investigated experimental conditions is less than 22% at a gas flow rate of 0.5 slm and a discharge power of 15 W and in most investigated cases $\sim 5\%$. This allows us, in first approximation, to neglect reduction in droplet diameter in the model. While the gas temperature of the plasma reaches up to 360 K, the droplet temperature remains significantly lower as can be estimated by (14). The temperature of a droplet of diameter 36 μm as a function of gas temperature is shown in Figure 9. The droplet temperature will be close to 300 K for the experimental conditions in this work and allows us to use reaction rates and transport coefficients at room temperature.

Assuming the rate of evaporation is constant, the flux of water into the plasma from a droplet of diameter 36 μm is estimated to be 2.5×10^{16} s^{-1}. As a reference, assuming the water vapor accumulates within 200 μm from the droplet, a local increase to $\sim$1% water vapor is possible. As the enhanced water vapor concentration will coincide with a sheath region depleted with electrons around the droplet, we anticipate a minimum impact of enhanced water vapor concentrations near the droplet (see Assumption 3).

Assumption 3: OH *and* H_2O_2 *diffuse from the bulk plasma to the droplet and decomposition reactions can be neglected during that process for the investigated experimental conditions.*

As droplets will be charged in the plasma, a sheath will be formed around the droplet which will repel electrons and will lead to a reduction of the OH density and production in this interfacial region which is dominantly produced by electron impact dissociation of water [44]. The OH radicals thus need to be transported from the bulk plasma across this sheath to the droplet. Figure 10 shows the calculation of the dimensionless radial distributions of OH and H_2O_2 densities near the gas-droplet interface for the 36 μm droplet at a residence time in the plasma of 10 ms.

While not considering the plasma sheath in the model, the calculated reduced OH and H_2O_2 density near the droplet surface becomes similar to the homogeneous OH and H_2O_2 density within a few droplet diameters, which is also the expected sheath size for an atmospheric pressure glow discharge [51]. Remarkably, the profile is similar for OH and H_2O_2, an illustrative example that OH transfer to the liquid phase is not limited by Henry's law. The diffusion time of OH from the bulk plasma to the droplet across a sheath of 200 μm can be estimated to be 8 μs [52]. The lifetime of the OH

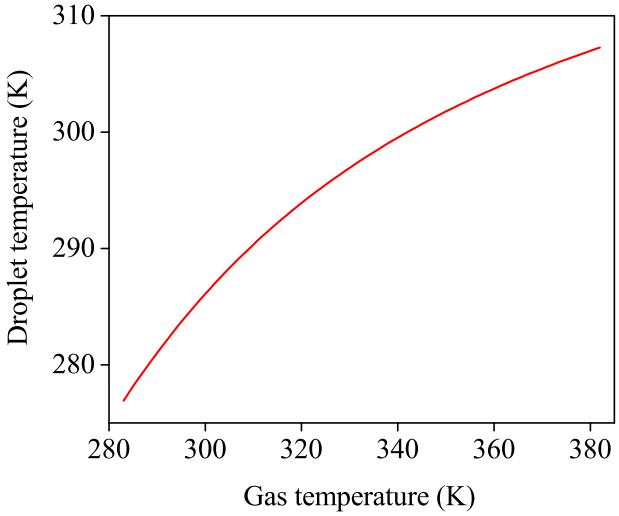

Figure 9. Theoretical droplet temperature versus gas temperature as calculated from (14) for a droplet of diameter 36 μm.

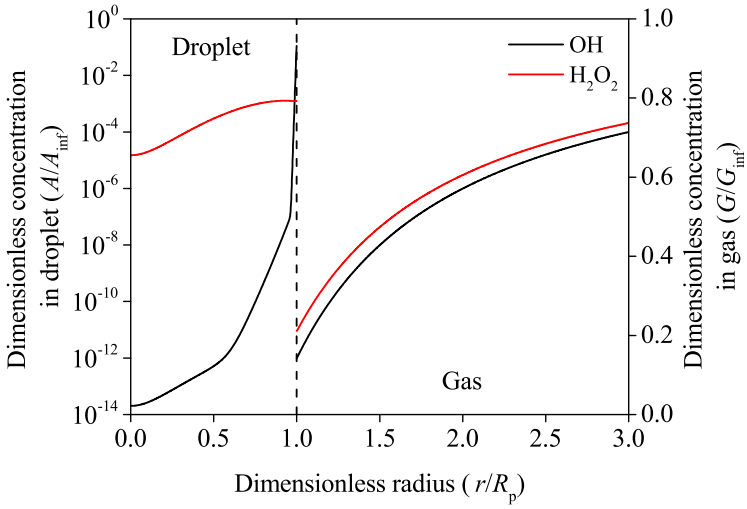

Figure 10. Radial distributions of OH and H_2O_2 densities near the gas-droplet interface for the 36 μm droplet. The distributions are shown for a droplet residence time of 10 ms in the plasma.

radical assuming an equal concentration of H and OH can be estimated by [53]

$$\frac{n_{\mathrm{OH}}}{n_{\mathrm{OH_0}}} = \frac{1}{1 + k_{\mathrm{loss}} n_{\mathrm{OH_0}} (t - t_0)}, \tag{18}$$

with k_{loss}, the combined reaction rate coefficient of quenching reactions with OH and H. (18) yields an OH lifetime of 0.17 ms for the investigated plasma conditions which is more than 20 times larger than the diffusion time. Hence, assuming a diffusion profile near the droplet will be a good first order approximation for calculating the flux of OH to the droplet. Similar arguments can be made for H_2O_2.

Assumption 4: *Convection inside the droplet does not significantly impact the oxidation of sodium formate.*

As convection typically proceeds on timescales larger than the lifetime of radicals, it is not expected to have an effect on the OH radicals. Nonetheless, it can play a role in the redistribution of the formate in the droplet when OH radicals are depleting the formate at the plasma-droplet interface. An estimate of the importance of convection compared to diffusion can be achieved through calculating the Peclet number ($\mathrm{Pe} = vLD^{-1}$), with v the liquid-phase velocity in the droplet and L the characteristic length of the sphere ($L = r/3$). Assuming that the maximum interfacial velocity will be equal to the relative velocity difference of the droplet compared to the surrounding gas $v \sim 0.4$ m/s. This yields a $\mathrm{Pe} \sim 10^3$ and hence convection is not negligible in steady state.

However, the residence time of the droplet in the plasma is at most 15 ms and no steady-state condition of convection in the droplet will be reached. A lower limit of the liquid phase convective time in the droplet, can be estimated from the maximal droplet velocity in the plasma. Indeed, the typical time of a single circulation of the liquid within the droplet can be estimated assuming that the liquid velocity is equal to the difference between the droplet velocity and gas velocity

$$\tau_{\mathrm{c}} = \frac{R}{\langle v \rangle} > \frac{R}{v_{\mathrm{max}}} = 30 \text{ ms}. \tag{19}$$

Hence, a convective vortex cannot be fully established when passing through the plasma and will have a minimal impact on the OH chemistry. Convection can, thus, also be neglected in the model and diffusion will be the dominant transport mechanism of formate during the plasma treatment.

5.2. Formate decomposition and species distributions in the droplet

Figure 8 compares the temporal evolution of the formate concentrations obtained by the calculation and the experiment. The excellent agreement with the experiment enables us to obtain further insights in the formate decomposition process by the model. Figure 11 shows the calculated radial profiles of the dominant liquid phase species for a droplet with a diameter of 36 μm and 56 μm and a droplet residence

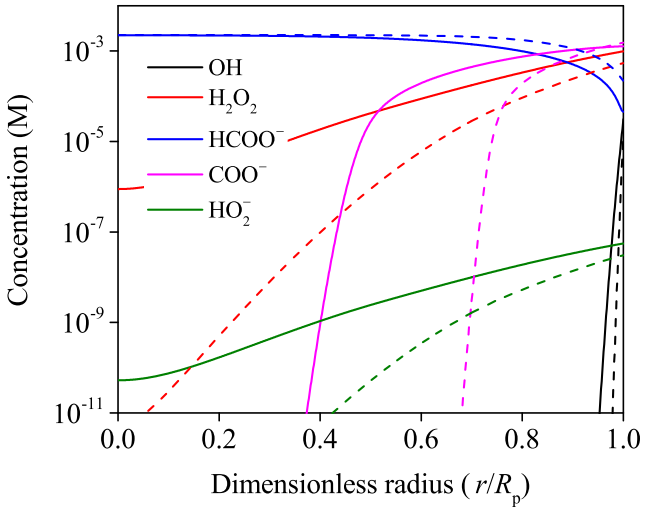

Figure 11. Radial profile of species in a droplet after 10 ms in plasma for droplet diameters of 36 μm (solid line) and 56 μm (dashed line).

time of 10 ms in the plasma. H_2O_2, a long-lived species, is able to penetrate the entire droplet of 36 μm, while significant penetration of OH is only found within 2 μm, causing a depletion of the formate near the interface. The radial profile of the formate concentration at the time equal to the residence time shows a clear gradient that extends significantly into the bulk of the droplet. Hence, formate is transported from the bulk of the droplet to the interface where it is decomposed by OH radicals. The formate concentration does drop significantly at the interface making COO^- the dominant species at later times (see Figure 11). However, not all decomposition products of formate have been included in the model as a complete reaction set is not available. Hence, the model could overestimate the decomposition of formate due to competing reactions with reaction products at larger exposure times. However, we believe the overall impact on the formate decomposition by this simplification will be relatively small because (1) the overall destruction of formate at later times (when products have the highest concentration) is limited, and (2) H_2O_2, a scavenger for OH, becomes one of the dominant species and at later times. Figure 12 and Figure 13 show the radial and temporal profiles of $HCOO^-$ concentration in a droplet, and the temporal variations of the aqueous phase concentrations of OH, H_2O_2 and $HCOO^-$ at the droplet interface, respectively. The OH concentration reaches a steady-state value at about 200 ns at the interface, while the depletion of the $HCOO^-$ concentration occurs at ms time scales. This drop in $HCOO^-$ concentration coincides with the formation of a gradient in the $HCOO^-$ concentration towards the bulk of the droplet

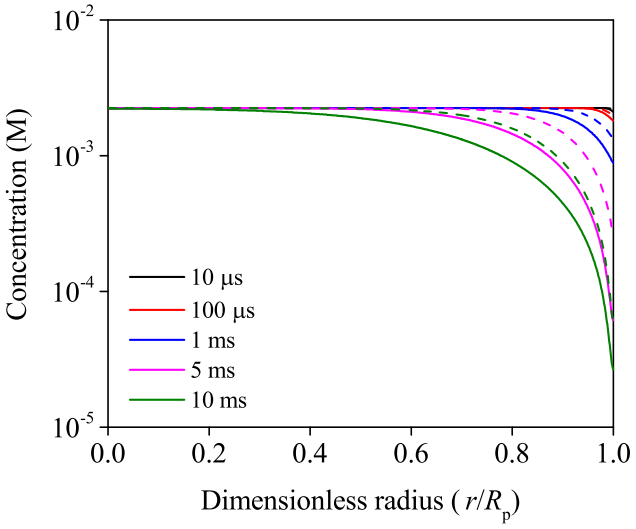

Figure 12. Radial and temporal profiles of $HCOO^-$ in a droplet for droplet diameters of 36 μm (solid line) and 56 μm (dashed line) droplet.

as shown in Figure 12, suggesting that the time-limiting step in the decomposition process of $HCOO^-$ is the diffusion of $HCOO^-$ from the bulk of the droplet to the interface. The diffusion limitation can also explain the less efficient removal of formate in a 56 μm droplet compared to a 36 μm droplet due to the increased diffusion time in the larger droplet.

Figure 12 can also explain the decreasing rates of the $HCOO^-$ decomposition with time as observed both in the model and the experiment in Figure 8. The formate concentration is quite low at the interface causing the diffusion of formate in the droplet towards the interface where it is being decomposed. The resulting diffusion profile extends further and further into the droplet as time develops. Hence, the unreacted formate needs to be transported over a larger distance from the center of the droplet to the interface to continue the conversion reaction, leading to a leveling off of the reduction rate of the averaged $HCOO^-$ concentration in the droplet with increasing time. Figure 13 shows that the OH concentration at the interface increases at a ms time scale as the concentration of $HCOO^-$ decreases. This leads to the increasing rate of H_2O_2 production because the dominant H_2O_2 production channel is through the recombination of OH radicals. Since the H_2O_2 concentration is not saturated even at $\sim$10 ms, increasing droplet residence time in the plasma would be beneficial to further enhance the H_2O_2 concentration.

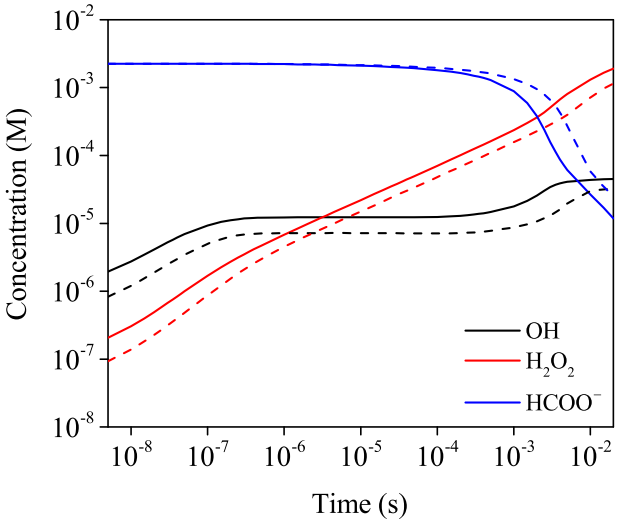

Figure 13. Liquid-phase concentration of OH, H_2O_2 and $HCOO^-$ on droplet surface for droplet diameters of 36 μm (solid line) and 56 μm (dashed line).

6. Conclusions

In this work, we reported a combined experimental and modeling study of a controlled plasma-droplet interaction experiment using a diffuse RF glow discharges in He + 0.2% H_2O. This approach allowed us, for the first time, to quantitatively study the reactivity transfer of OH from the gas phase plasma to the liquid phase. The droplet residence time and change in droplet diameter in the plasma were determined by microscopic fast framing imaging. The droplet diameter reduction could be explained by a standard droplet evaporation model based on gas heating by the plasma. The gas temperature and gas-phase densities of OH and H_2O_2 were experimentally determined in the plasma and formate concentrations were measured in droplets collected after treated by the plasma. We observed 50% reduction in formate concentration in the droplets after plasma treatment for droplet residence times in the plasma of $\sim$10 ms.

A one-dimensional model was used to calculate the OH transport and formate oxidation inside the droplet. This simple 1D reaction-diffusion model is able to predict the conversion of formate by plasma in a droplet without any fitting parameters. The model further shows that formate conversion is dominated by near-interfacial reactions with OH radicals and is highly diffusion limited. This also explains why the formate decomposition efficiency is reducing for increasing droplet residence times in the plasma. The results show that a controlled plasma-micro-droplet reactor as reported in this study might be an excellent tool for detailed quantitative plasma-

liquid interaction studies.

Acknowledgments

This material is based upon work supported by the National Science Foundation (PHYS 1903151) and the US Department of Energy, Office of Science, Office of Fusion Energy Sciences under award number DE-SC0001939. The authors thank Prof. M Kushner (U of Michigan) for helpful discussions on plasma-droplet interactions.

References

[1] Bruggeman P J, Kushner M J, Locke B R, Gardeniers J G, Graham W, Graves D B, Hofman-Caris R, Maric D, Reid J P, Ceriani E *et al.* 2016 *Plasma Sources Science and Technology* **25** 053002

[2] Adamovich I, Baalrud S D, Bogaerts A, Bruggeman P, Cappelli M, Colombo V, Czarnetzki U, Ebert U, Eden J G, Favia P *et al.* 2017 *Journal of Physics D: Applied Physics* **50** 323001

[3] Starikovskiy A, Yang Y, Cho Y I and Fridman A 2011 *Plasma Sources Science and Technology* **20** 024003

[4] Tachibana K, Takekata Y, Mizumoto Y, Motomura H and Jinno M 2011 *Plasma Sources Science and Technology* **20** 034005

[5] Foster J E, Weatherford B, Gillman E and Yee B 2010 *Plasma Sources Science and Technology* **19** 025001

[6] Burlica R and Locke B R 2008 *IEEE Transactions on Industry Applications* **44** 482–489

[7] Ratner B D 1993 *Journal of Biomaterials Science, Polymer Edition* **4** 3–11

[8] Martin P M 2009 *Handbook of deposition technologies for films and coatings: science, applications and technology* (William Andrew)

[9] Fauchais P, Etchart-Salas R, Rat V, Coudert J F, Caron N and Wittmann-Ténèze K 2008 *Journal of Thermal Spray Technology* **17** 31–59

[10] Fauchais P, Joulia A, Goutier S, Chazelas C, Vardelle M, Vardelle A and Rossignol S 2013 *Journal of Physics D: Applied Physics* **46** 224015

[11] Goree J 1994 *Plasma Sources Science and Technology* **3** 400

[12] Bonitz M, Henning C and Block D 2010 *Reports on Progress in Physics* **73** 066501

[13] Khrapak S, Ivlev A, Morfill G and Thomas H 2002 *Physical Review E* **66** 046414

[14] Maguire P, Rutherford D, Macias-Montero M, Mahony C, Kelsey C, Tweedie M, Pérez-Martin F, McQuaid H, Diver D and Mariotti D 2017 *Nano letters* **17** 1336–1343

[15] Merche D, Vandencasteele N and Reniers F 2012 *Thin Solid Films* **520** 4219–4236

[16] Iqbal M M, Stallard C P, Dowling D P and Turner M M 2015 *Plasma Processes and Polymers* **12** 201–213

[17] Kruszelnicki J, Lietz A M and Kushner M J 2019 *Journal of Physics D: Applied Physics* **52** 355207

[18] Machala Z, Tarabova B, Hensel K, Spetlikova E, Sikurova L and Lukes P 2013 *Plasma Processes and Polymers* **10** 649–659

[19] Maguire P, Mahony C, Kelsey C, Bingham A, Montgomery E, Bennet E, Potts H, Rutherford D, McDowell D, Diver D *et al.* 2015 *Applied Physics Letters* **106** 224101

[20] Bennet E, Mahony C M, Potts H E, Everest P, Rutherford D, Askari S, McDowell D, Mariotti D, Kelsey C, Perez-Martin F *et al.* 2016 *Journal of Aerosol Science* **100** 53–60

[21] Liu D, Liu Z, Chen C, Yang A, Li D, Rong M, Chen H and Kong M 2016 *Scientific Reports* **6** 23737

[22] Anderson C E, Cha N R, Lindsay A D, Clark D S and Graves D B 2016 *Plasma Chemistry and Plasma Processing* **36** 1393–1415

[23] Wende K, Williams P, Dalluge J, Van Gaens W, Aboubakr H, Bischof J, Von Woedtke T, Goyal S M, Weltmann K D, Bogaerts A *et al.* 2015 *Biointerphases* **10** 029518

[24] Norberg S A, Tian W, Johnsen E and Kushner M J 2014 *Journal of Physics D: Applied Physics* **47** 475203

[25] Stratton G R, Dai F, Bellona C L, Holsen T M, Dickenson E R and Mededovic Thagard S 2017 *Environmental Science & Technology* **51** 1643–1648

[26] Franclemont J, Fan X and Thagard S M 2015 *Journal of Physics D: Applied Physics* **48** 424004

[27] Chen C, Liu D, Liu Z, Yang A, Chen H, Shama G and Kong M 2014 *Plasma Chemistry and Plasma Processing* **34** 403–441

[28] Rumbach P, Bartels D M, Sankaran R M and Go D B 2015 *Nature Communications* **6** 1–7

[29] Nayak G, Sadeghi N and Bruggeman P J 2019 *Plasma Sources Science and Technology* **28** 125006

[30] Hofmann S, Van Gessel A, Verreycken T and Bruggeman P 2011 *Plasma Sources Science and Technology* **20** 065010

[31] Schneider C A, Rasband W S and Eliceiri K W 2012 *Nature Methods* **9** 671–675

[32] Bruggeman P, Cunge G and Sadeghi N 2012 *Plasma Sources Science and Technology* **21** 035019

[33] Bruggeman P J, Sadeghi N, Schram D and Linss V 2014 *Plasma Sources Science and Technology* **23** 023001

[34] Du Y, Nayak G, Oinuma G, Ding Y, Peng Z and Bruggeman P J 2017 *Plasma Sources Science and Technology* **26** 095007

[35] Eisenberg G 1943 *Industrial & Engineering Chemistry Analytical Edition* **15** 327–328

[36] Crapulli F, Santoro D, Sasges M and Ray A 2014 *Water Research* **64** 209–225

[37] Imoberdorf G and Mohseni M 2011 *Chemical Engineering Science* **66** 1159–1167

[38] Mai H, Shiraiwa M, Flagan R C and Seinfeld J H 2015 *Environmental Science & Technology* **49** 11485–11491

[39] Liu Y, Ivanov A V and Molina M J 2009 *Geophysical Research Letters* **36**

[40] Ivanov A V, Trakhtenberg S, Bertram A K, Gershenzon Y M and Molina M J 2007 *The Journal of Physical Chemistry A* **111** 1632–1637

[41] Sander R 2015 *Atmospheric Chemistry and Physics* **15** 4399–4981

[42] Roeselová M, Vieceli J, Dang L X, Garrett B C and Tobias D J 2004 *Journal of the American Chemical Society* **126** 16308–16309

[43] Davidovits P, Kolb C E, Williams L R, Jayne J T and Worsnop D R 2006 *Chemical Reviews* **106** 1323–1354

[44] Vasko C, Liu D X, Van Veldhuizen E, Iza F and Bruggeman P J 2014 *Plasma Chemistry and Plasma Processing* **34** 1081–1099

[45] Hinds W C 1999 *Aerosol technology: properties, behavior, and measurement of airborne particles* (John Wiley & Sons)

[46] Liu D X, Bruggeman P, Iza F, Rong M Z and Kong M G 2010 *Plasma Sources Science and Technology* **19** 025018

[47] Locke B R and Shih K Y 2011 *Plasma Sources Science and Technology* **20** 034006

[48] Rumble J R 2016 Nist 40. ndrl/nist solution kinetics database: Version 3.0 Tech. rep.

[49] Golda J, Biskup B, Layes V, Winzer T and Benedikt J 2020 *Plasma Processes and Polymers* e1900216

[50] Chirokov A, Khot S, Gangoli S, Fridman A, Henderson P, Gutsol A and Dolgopolsky A 2009 *Plasma Sources Science and Technology* **18** 025025

[51] Shi J and Kong M G 2005 *IEEE Transactions on Plasma Science* **33** 624–630

[52] Alvarez N J, Walker L M and Anna S L 2010 *Physical Review E* **82** 011604

[53] Verreycken T, Van der Horst R, Baede A, Van Veldhuizen E and Bruggeman P 2012 *Journal of Physics D: Applied Physics* **45** 045205